Optimization of Parameter Values in the Turbulence Model Aided by Data Assimilation

Hiroshi Kato,* Keiichi Ishiko,† and Akira Yoshizawa‡

Japan Aerospace Exploration Agency, Tokyo 182-8522, Japan

This study proposes a data assimilation methodology for estimating the optimal parameter values of turbulence models. The proposed methodology was applied to the estimation of the parameter a_1 in the modified Menter k-ω shear-stress transport turbulence model. For this purpose, a fundamental turbulent flow, namely, the flow over a two-dimensional backward-facing step, was employed. The estimated value of a_1 (1.0) differed from its original value (i.e., 0.31). The modified Menter k-ω shear-stress transport turbulence model with $a_1 = 1.0$ was validated on several turbulent flow calculations; flows over a two-dimensional backward-facing step and a two-dimensional flat-plate boundary layer, two-dimensional transonic flows around the RAE 2822 airfoil, and three-dimensional transonic flows around the ONERA M6 wing. In simulations, the modified Menter k-ω shear-stress transport turbulence model with $a_1 = 1.0$ better modeled the separated and adverse pressure gradient flows than the original modified Menter k-ω shear-stress transport turbulence model with $a_1 = 0.31$. Furthermore, in the absence of separation and adverse pressure gradient flows, the proposed and original modified Menter k-ω shear-stress transport turbulence models computed almost the same results. These observations suggest that the proposed data assimilation methodology effectively estimates the optimal parameter values of turbulence models and that the estimated a_1 (1.0) improves the performance of the modified Menter k-ω shear-stress transport turbulence model over the original value (i.e., 0.31).

Nomenclature

k	=	turbulent kinetic energy
P	=	production term of the Menter k-ω shear-stress transport turbulence model
ν_t	=	eddy viscosity
γ	=	specific heat ratio
μ_t	=	turbulent eddy viscosity
μ	=	molecular dynamic viscosity
ω	=	specific dissipation

I. Introduction

EDDY-VISCOSITY-TYPE turbulence models, especially the Spalart–Almaras (SA) turbulence model [1] and the Menter k-ω shear-stress transport (SST) turbulence model [2], have been widely employed in engineering applications of computational fluid dynamics (CFD). Furthermore, several researchers have modified the SA and SST models to better simulate complicated turbulent flows. Previous improvements have been well summarized in the turbulence modeling resource of NASA's Langley Research Center.

This study aims to improve the SST model modified by Menter et al. in 2003 [3] (SST-2003 model). Unlike the previous approaches, which have modified the formulas of the adopted turbulence models, the present study changes only the value of the parameter a_1 in the SST-2003 model. Thus, it presents a much simpler approach than previous efforts.

*Researcher, Institute of Aeronautical Technology, Chofu; kato.hiroshi@jaxa.jp. Member AIAA.

†Invited Researcher, Institute of Aeronautical Technology, Chofu; ishiko.keiichi@jaxa.jp. Member AIAA.

‡Visiting Researcher, Institute of Aeronautical Technology, Chofu; ay-tsch@mbg.nifty.com.

The SST model is formulated as follows:

$$\nu_t = \frac{a_1 k}{\max(a_1 \omega, \Omega F_2)} \quad (1)$$

$$\frac{\partial(\rho k)}{\partial t} + \frac{\partial(\rho u_j k)}{\partial x_j} = P - \beta^* \rho k \omega + \frac{\partial}{\partial x_j}\left[(\mu + \sigma_k \mu_t)\frac{\partial k}{\partial x_j}\right] \quad (2)$$

$$\frac{\partial(\rho \omega)}{\partial t} + \frac{\partial(\rho u_j \omega)}{\partial x_j} = \frac{\gamma}{\nu_t} P - \beta^* \rho \omega^2 + \frac{\partial}{\partial x_j}\left[(\mu + \sigma_\omega \mu_t)\frac{\partial \omega}{\partial x_j}\right]$$
$$+ 2(1 - F_1)\frac{\rho \sigma_{\omega 2}}{\omega}\frac{\partial k}{\partial x_j}\frac{\partial \omega}{\partial x_j} \quad (3)$$

The baseline of the SST model is the k-ε model, and the blending functions F_1 and F_2 switch between the k-ε model for flows away from the boundary layer and the k-ω model for flows inside the boundary layer. The blending functions F_1 and F_2 are, respectively, defined as follows:

$$F_1 = \tanh\left\{\left\{\min\left[\max\left(\frac{\sqrt{k}}{\beta^* \omega y}, \frac{500\nu}{y^2 \omega}\right), \frac{4\rho \sigma_{\omega 2} k}{CD_{k\omega} y^2}\right]\right\}^4\right\} \quad (4)$$

$$F_2 = \tanh\left[\left[\max\left(\frac{2\sqrt{k}}{\beta^* \omega y}, \frac{500\nu}{y^2 \omega}\right)\right]^2\right] \quad (5)$$

Equation (6) is the switching function by which the blending function F_1 switches the constants in the SST-2003 model. F_1 equals zero and 1 for flows distant from the boundary layer and inside the boundary layer, respectively:

$$\phi = F_1 \phi_1 + (1 - F_1)\phi_2 \quad (6)$$

In Eq. (6), ϕ_i represents the constants ($\sigma_{ki}, \sigma_{\omega i}, \beta_i, \gamma_i$), where $i = 1$, and 2, and ϕ represents the constants ($\sigma_k, \sigma_\omega, \beta, \gamma$). The constants in the original SST-2003 model were assigned as follows:

$$\sigma_{k1} = 0.85, \qquad \sigma_{\omega 1} = 0.5, \qquad \beta_1 = 3/40, \qquad \gamma_1 = 5/9,$$

$$\sigma_{k2} = 1, \qquad \sigma_{\omega 2} = 0.856, \qquad \beta_2 = 0.0828, \qquad \gamma_2 = 0.44$$

$$\beta^* = 0.09, \qquad \kappa = 0.41, \qquad a_1 = 0.31 \tag{7}$$

The second blending function F_2 affects the computed turbulent eddy viscosity. The SST-2003 model is detailed in [2,3].

The SST-2003 and original SST models differ mostly in their evaluations of the turbulent viscosity. In the SST-2003 model, the turbulent viscosity is calculated by Eq. (8), in which the absolute value of the vorticity Ω in Eq. (1) is replaced by the invariant measure of the strain rate S:

$$\nu_t = \frac{a_1 k}{\max(a_1 \omega, SF_2)} \tag{8}$$

Some of the preceding constants have been analytically determined under certain assumptions of fundamental turbulent flows; others have been empirically determined by matching model results to experimental or computational flow data [4]. The current study optimizes the value of the parameter a_1, which is involved in the turbulent viscosity formulas [Eqs. (1) and (8)]. These equations, which describe the advection effect of turbulent stress, were recognized as representative of adverse pressure gradient flows in the study of the SST model [2]. Furthermore, these equations are based on the Johnson–King turbulence model [5], the first model of the advection effect of turbulent stress. The value assigned to a_1 in the SST model (0.31) was consistent with a study on the Johnson–King turbulence model, in which a_1 was observed to vary between 0.2 and 0.3. However, note that that the formula involving a_1 differs between the Johnson–King turbulence and SST models. Furthermore, as described previously, the SST and SST-2003 models differ in their turbulent viscosity formulations.

Given the preceding observations, the value a_1 in the SST-2003 model is worthy of further investigation. If the value of a_1 can be improved from its original value (i.e., 0.31), the SST-2003 model will better reproduce adverse pressure gradient flows. In addition, changing the value of a_1 alone is advantageous because completely nonadverse pressure gradient flows are independent of this parameter. Specifically, in the absence of adverse pressure gradient flows, a_1 enters the denominator of Eq. (8) and cancels a_1 in the numerator. Therefore, by modifying a_1, we alter only the adverse pressure gradient flows, and the reliability of the SST-2003 model in the absence of adverse pressure gradient flows is unchanged.

The present study uses a data assimilation methodology [6] to determine the values of turbulence model parameters. Data assimilation originated in meteorology research and has been widely used to estimate the initial and boundary conditions in numerical weather predictions. The present study employs an ensemble transform Kalman filter (ETKF) [7], an extended Kalman filter for nonlinear system models that can be represented by Bayesian estimations.

To investigate the value of a_1 in the SST-2003 model, we model the flow over a backward-facing step. This fundamental turbulent flow, reported by Driver and Seegmiller [8], is frequently used to validate turbulence models [9]. Many such validations have been reported in the turbulence modeling resource developed by NASA Langley Research Center. According to these validations, turbulence models cannot replicate the observed complicated characteristics of turbulent flows, such as separation, reattachment, and adverse pressure gradient flows, which can be regarded as reliable. The observations further suggest that the optimal value of a_1 is best estimated by modeling the flow over a backward-facing step. Optimizing this parameter would improve the ability of SST-2003 to model complicated turbulent flows. Finally, the effectiveness of the estimated value of a_1 is evaluated in calculations of several turbulent flows.

The rest of the paper is organized as follows. Section II describes the methodology, and Sec. III discusses the experimental data used in the data assimilation. The process of data assimilation is shown in Sec. IV. Sections V and VI present the results and conclusions, respectively.

II. Method

Data assimilation methods are divided into two types. The first type, based on Bayesian estimation, is typified by the ensemble Kalman filter (EnKF) [10] and the particle filter [11] methods. The second type, based on the maximum-likelihood estimation, is represented by the four-dimensional variational method [12]. In this study, the ETKF was adopted as the data assimilation method. Like the EnKF, the ETKF belongs to the first category of data assimilation methods. This section describes the ETKF-based data assimilation framework.

A. Extended State-Space Model

The state-space model is a major component of the data assimilation framework. The state-space model consists of an observation model and a system model as follows:

$$x_t = f(x_{t-1}, v_t) \tag{9}$$

$$y_t = H x_t + w_t \tag{10}$$

Equations (9) and (10) represent the system and observation models, respectively. In both equations, the vectors x_t and y_t denote the state vectors of the system model and the experimental data, respectively, at time t. The vectors v_t and w_t denote the system and experimental noises, respectively. The nonlinear operator f in Eq. (9) represents the temporal evolution from time $t - 1$ to time t in simulations. The linear operator H in Eq. (10), called the observation matrix, projects the state vector x_t on the experimental space. The system noise v_t is ignored in the present study.

The state vector of the system model was originally defined as follows:

$$x_t = (\xi_1^T, \xi_2^T, \xi_3^T, \ldots, \xi_M^T)^T \tag{11}$$

$$\xi_i = (\rho_i, u_i, v_i, p_i, k_i, \omega_i)^T \tag{12}$$

where ξ represents the state variables defined on each computational grid point, and ρ, u, v, and p denote the density, inflow horizontal and vertical velocity components in the inflow direction, and pressure, respectively. In Eq. (12), k and ω denote the variables that solve the Menter k-ω SST turbulence model. The superscript T indicates the transposed matrix, and the subscript M indicates the number of computational grid points.

The value of the parameter a_1 to be optimized is input to the system model. Because the original state vector Eq. (11) is unsuitable for this study, it is extended to Eq. (13):

$$x_t = (\xi_1^T, \xi_2^T, \xi_3^T, \ldots, \xi_M^T, a_1)^T \tag{13}$$

This extended state vector enables the estimation of a_1 under the data assimilation framework.

B. System Model

The system model is a CFD code called the fast aerodynamic routine (FaSTAR) [13], developed at the Japan Aerospace Exploration Agency. The FaSTAR solves the compressible Navier–Stokes equations on an unstructured grid using the cell-centered finite volume method.

The flow over a backward-facing step was simulated under the following flow conditions: Reynolds number = 36,000, Mach number = 0.128, and temperature = 537°R. These flow conditions are adopted in flows over two-dimensional (2-D) backward-facing steps in the turbulence modeling resource developed by NASA Langley Research Center.

The FaSTAR has been implemented in several computational methods. In this computation, the inviscid flux term was computed by simple low-dissipation Advection Upstream Splitting Method (AUSM) [14], and the time integration was implicitly performed by
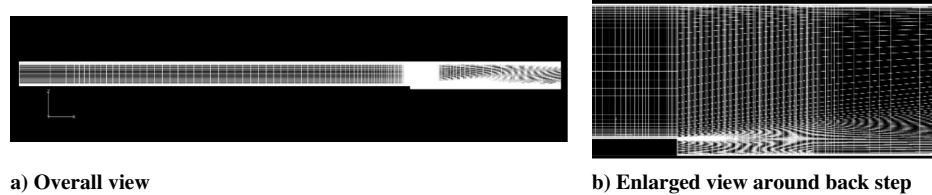
a) Overall view   b) Enlarged view around back step

Fig. 1   Computational grid.

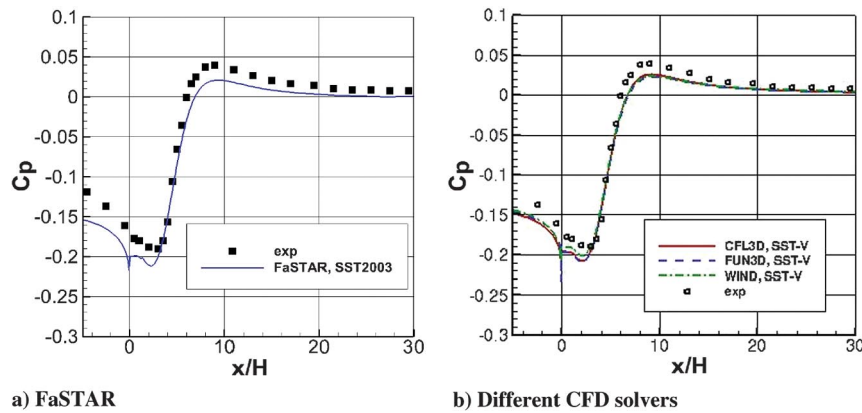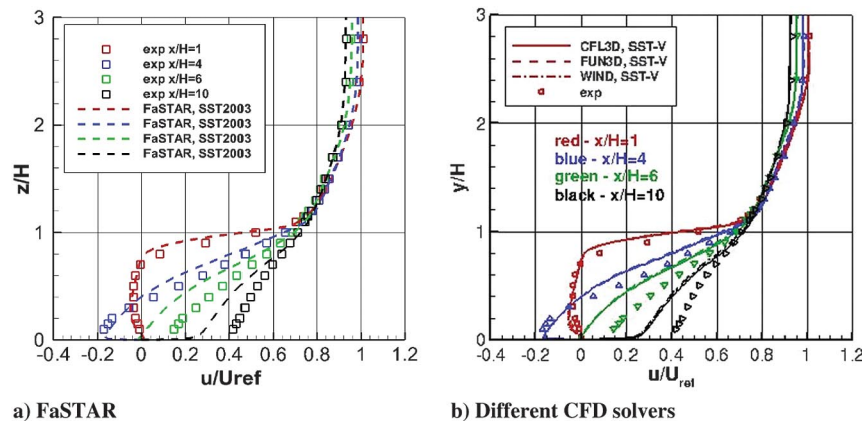a) FaSTAR   b) Different CFD solvers

Fig. 2   Comparison of backstep C_p computed by various solvers. Figure 2b is available from the turbulence modeling resource developed by NASA Langley Research Center.

a) FaSTAR   b) Different CFD solvers

Fig. 3   Comparison of backstep velocity profiles computed by various solvers. Figure 3b is available from the turbulence modeling resource developed by NASA Langley Research Center.

the preconditioned lower/upper symmetric Gauss–Seidel method [15]. The time integration was performed using local time stepping, and the gradients were calculated to second-order spatial accuracy by Green–Gauss-based weighted least square (GLSQ) [16] with Hishida's limiter. The turbulence model in this computation was the Menter k-ω SST turbulence model modified by Menter et al. in 2003 (SST-2003) [3].

Simulations were run on a three-dimensional (3-D) unstructured grid (two identical x-z planes separated by a distance $y = 1$, giving one spanwise cell for all grid levels), as shown in Fig. 1. The grid was constructed from 40,594 nodes and 19,968 elements, and the minimum spacing of the surface normal in the wall units was approximately 6.0d-4. The grid employed in this computation is available in the turbulence modeling resource developed by NASA Langley Research Center. The effects of minimum surface normal spacing on the computational results were investigated before computation.

Figures 2 and 3 plot the experimental and computed backstep pressure coefficient C_p data and velocity profiles, respectively. In Figs. 2 and 3 H denotes the step height, exp denotes the experimental data from Driver and Seegmiller [8], and SST2003 and SST-V are the names of the turbulence models employed in the computation. In

Fig. 3, results are compared at locations downstream of the step: $x/H = 1$, 4, 6, and 10. In these figures, FaSTAR is validated by comparing its results to those of various CFD solvers, namely CFL3D, FUN3D, and WIND. The computational results of the three CFD solvers are available in the turbulence modeling resource developed by NASA Langley Research Center.§ The results of FaSTAR and the different CFD solvers nearly coincide. However, like the CFD solvers, FaSTAR largely fails to represent the experimental velocity profiles at locations far from the step (i.e., at $x/H = 6$ and 10).

C. Observation Model

The experimental data y_t in the observation model were the experimental horizontal and vertical velocity profiles reported by Driver and Seegmiller [8]. These authors measured the velocity profiles at widely distributed points in the flow region. To validate the computational results in the turbulence modeling resource of NASA's Langley Research Center, we here extracted the experimental data

---

§Data available online at http://turbmodels.larc.nasa.gov/backstep_val. html [retrieved 12 August 2014].

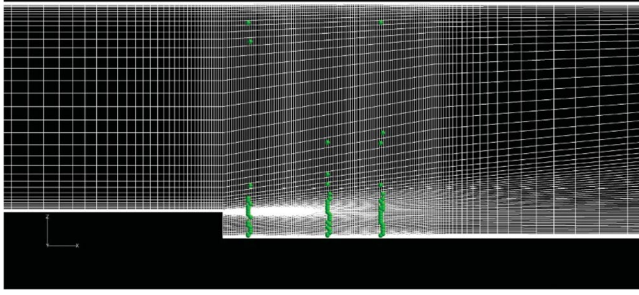**Fig. 4   Locations of experimental data.**

located at $x/H = -4$, 1, 4, 6, and 10 from Driver and Seegmiller's study. In addition, only the experimental data near the computational grid points were employed in the data assimilation. More specifically, the data assimilation used 124 experimental data measured downstream of the step. The locations of the experimental data are indicated in Fig. 4.

The linear operator H in the observation model is defined as

$$
H = \begin{pmatrix} 1 & & & \\ & & 1 & \\ & & & 1 \\ 1 & & & \\ & 1 & & \end{pmatrix}
\tag{14}
$$

H is an $(l \times k)$-dimensional matrix of l experimental data and k state variables. The elements of H are 1 (if the grid location corresponds to a measurement location) or 0.

D.   Ensemble Transform Kalman Filter

The ETKF is a nonlinear version of the Kalman filter (KF) [17]. Before describing the ETKF, this subsection briefly introduces the KF and two standard nonlinear variants (i.e., the extended Kalman filter [18] and the EnKF).

The KF adopts the minimum error variance assumption and involves a weight matrix called the Kalman gain, calculated by Eq. (15). The optimum state vector is derived from the data of the system and observation models by Eq. (17):

$$
K_t = V_t^f H^T (H V_t^f H^T + R_t)^{-1}
\tag{15}
$$

$$
V_t^a = (I - K_t H) V_t^f
\tag{16}
$$

$$
x_t^a = x_t^f + K_t (y_t - H x_t^f)
\tag{17}
$$

where V_t^f and R_t denote the variance–covariance matrices of the state vector and the experimental noise. The superscripts f and a in Eqs. (15–20) indicate the background prior distribution calculated from the system model and the posterior distribution in the analysis, respectively.

The KF was derived from linear problems and so is unsuited to nonlinear problems. Therefore, several nonlinear variants of the KF have been developed. A representative nonlinear version of the KF is the ETK, which calculates the Kalman gain and the variance–covariance matrices of the state vector from linear approximations to the original nonlinear system and observational models. However, strongly nonlinear and high-dimensional system models, such as the evolution of nonphysical error variances and problems incurring large computational load (e.g., [19]), are difficult to handle by the EFK.

In 1994, Evensen [10] proposed the EnKF as an alternative method to linearize the system model. In the EnKF, the filtered mean and variance of the KF are replaced by a set of obtained ensemble members. The mean matrix of ensemble members $\hat{X}_t^f$ and the variance–covariance matrix of ensemble members $\hat{V}_t^f$ are represented as follows:

$$
\hat{X}_t^f = \frac{1}{N} X_t^f 1_{N \times N}
\tag{18}
$$

$$
\delta X_t^f = X_t^f - \hat{X}_t^f
\tag{19}
$$

$$
\hat{V}_t^f = \frac{1}{N-1} \delta X_t^f (\delta X_t^f)^T
\tag{20}
$$

where N is the number of ensemble members. In the preceding equations, X_t^f is the N-dimensional matrix of the state variables x_t^f of ensemble members, defined as follows:

$$
X_t^f = (x_t^{f(1)} \quad x_t^{f(2)} \quad \cdots \quad x_t^{f(N)})
\tag{21}
$$

In Eq. (21), the superscripts (1), (2), ..., (N) are the indices of the ensemble members. We also define $1_{N \times N}$ as an $N \times N$ matrix of ones:

$$
1_{N \times N} = \begin{pmatrix} 1 & 1 & \cdots & 1 \\ 1 & 1 & & \vdots \\ \vdots & & \ddots & \vdots \\ 1 & \cdots & \cdots & 1 \end{pmatrix}
\tag{22}
$$

Many researchers have demonstrated the effectiveness of the EnKF and have proposed a range of EnKF variants. Among these variants is the ensemble transformed Kalman filter (ETKF), which is derived from the square root filter [20]. The ETKF is advantaged by lower calculation cost than other EnKF variants [21], rendering it specifically suited to aeronautical flow analysis, which incurs massive calculation costs.

The ETKF proceeds by the following equations.

$$
I + \delta X_t^{fT} H_t^T [(N-1)R_t]^{-1} H_t \delta X_t^f = Z \Sigma Z^T
\tag{23}
$$

$$
\hat{K}_t = \delta X_t^f Z \Sigma^{-1} Z^T \delta X_t^{fT} H_t^T [(N-1)R_t]^{-1}
\tag{24}
$$

$$
T = Z \Sigma^{-1/2} Z^T
\tag{25}
$$

$$
\hat{X}_t^a = \hat{X}_t^f + \hat{K}_t (Y_t - H_t \hat{X}_t^f)
\tag{26}
$$

$$
\delta X_t^a = \delta X_t^f T
\tag{27}
$$

$$
X_t^a = \hat{X}_t^a + \delta X_t^a
\tag{28}
$$

In the left-hand side of Eq. (23), I and R_t represent the unit matrix and the variance–covariance matrix, respectively, of the experimental noise w_t. R_t was calculated from the experimental noise w_t acquired from random numbers from normal distribution with mean of 0.0 and variance of 1.0d-6, $N(0, 1.0d-6)$. Z and Σ on the right-hand side of Eq. (23) denote the eigenvectors and eigenvalues of the left-hand side, respectively, computed by singular value decomposition. The quantity $\hat{K}_t$ on the left-hand side of Eq. (24) denotes the Kalman gain. On the right-hand side of Eq. (26), the N-dimensional matrix Y_t contains the experimental values of the ensemble members $y_t^{(i)} (i = 1, \ldots, N)$, which are identical for each ensemble member. Superscripts -1 and $-1/2$ indicate the inverse matrix and its square root, respectively. The inverse matrix was computed by singular value decomposition.

Equations (23–28) optimize the a_1 value of each ensemble member.
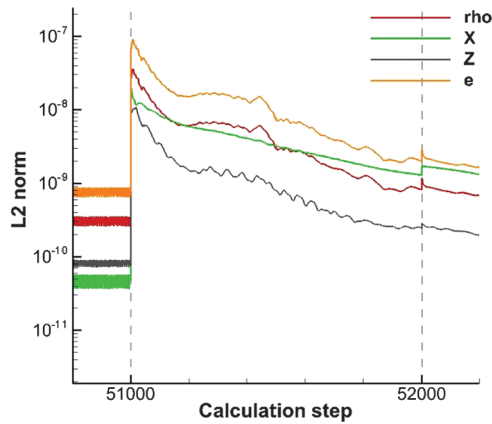
Fig. 5 Histories of residual norms of squares (L2 norms). The red, green, gray, and orange lines represent the density, momentum in the horizontal and vertical direction, and energy, respectively.

E. Data Assimilation Process

This subsection details the data assimilation process. The data assimilation process consists of two main steps: a prediction step and a filtering step.

In the first step of data assimilation, a set of initial ensemble members is prepared. This set represents the prior distribution of the system model. Because this study aimed to estimate the optimal value of a_1, the prior distribution of the system model was easily prepared, and different parameter values were assigned to the computational conditions of the ensemble members. The value of a_1 was selected from 0.04 to 1.2, and the prior distribution of the system model was derived from 30 ensemble members.

In the second step, the value of a_1 was estimated by data assimilation. This filtering step was iterated 40 times to ensure a good data assimilation result. The filtering steps were intercalated with prediction steps, which performed CFD calculations using the a_1 value estimated by the prior filtering step. The number of calculations in each prediction step (1000) was adjusted to ensure that the residual norms of squares (L2 norms) of the densities, momenta, and energies immediately after the filtering step dropped to below 10% of their values before the next filtering step. Meanwhile, the number of filtering steps (40) ensured that the mean of the estimated a_1 values of the ensemble members converged. Figure 5 shows the histories of the L2 norms of the density, momentum, and energy for an ensemble member. The L2 norms increase after the first filtering step of 51,000 calculation steps. As shown in this figure, the L2 norms drop to less than 10% of their previous values within 1000 calculation steps following the 51,000th calculation.

The data assimilation process can be summarized as follows.
1) Determine the initial ensemble members.

2) Start the data assimilation iterations, and set $t^* \leftarrow 1$ (where t^* indicates the number of iterations of the data assimilation).
   3) At t^*,
      a) Prediction step: calculate 1000 CFD steps for each ensemble member.
      b) Filtering step: calculate the posterior distributions from the ETKF Eqs. (14–19).
   4) Set $t^* \leftarrow t^* + 1$, and repeat step 3 until $t^* = 40$.
   5) Obtain the optimum value of the parameter a_1.

III.   Results

This section presents the data assimilation results and validates the estimated value of a_1. The validity of the method is demonstrated in CFD calculations of several flow problems, namely flows over a 2-D backward-facing step and a flat-plate boundary layer, 2-D transonic flow around the RAE 2822 airfoil, and 3-D transonic flow around the ONERA M6 wing.

A.   Data Assimilation Results

First, the effectiveness of the data assimilation framework at estimating a_1 was evaluated in a numerical experiment. The true value of the parameter a_1 was known and was used to generate pseudoexperimental data. If the data assimilation can effectively estimate the value of a_1, it can estimate the true value. In this study, the true value was set to the original value (i.e., 0.31), and the pseudoexperimental data were extracted from flows using the true value, at the locations of the actual data assimilation shown in Fig. 4. As implemented in the actual data assimilation, the noise in the pseudoexperimental data was randomized within the range $N(0, 1.0d - 6)$. Similarly, the a_1 values of the ensemble members were initialized to their initial values in the data assimilation.

Figure 6 plots the mean and variance estimation histories of the a_1 values of the ensemble members. Figure 7 shows the histograms of the a_1 values of the ensemble members before and after estimation. The means and variances of the a_1 values of the ensemble members before and after estimation are presented in Table 1.

Comparing the a_1 values before and after estimation, we determine that 1) the estimated a_1 values of the ensemble members converge to a narrower range than the initial values, and 2) the mean of the estimated a_1 values of the ensemble members almost matches the true value.

According to this observation, the proposed data assimilation framework effectively estimates the optimal value of a_1 through the employed experimental data.

Next, the data assimilation was trialed on actual experimental data. The data assimilation results are presented in Figs. 8 and 9 and Table 2. As evident in Figs. 8b and 9b and Table 2, the estimated a_1 values of the ensemble members converge differently from the numerical experiment. This indicates that the a_1 value has a high degree of freedom for the optimum value. In addition, Fig. 8a confirms that the mean of the estimated a_1 values converge to 1.0, whereas the original value is 0.31.
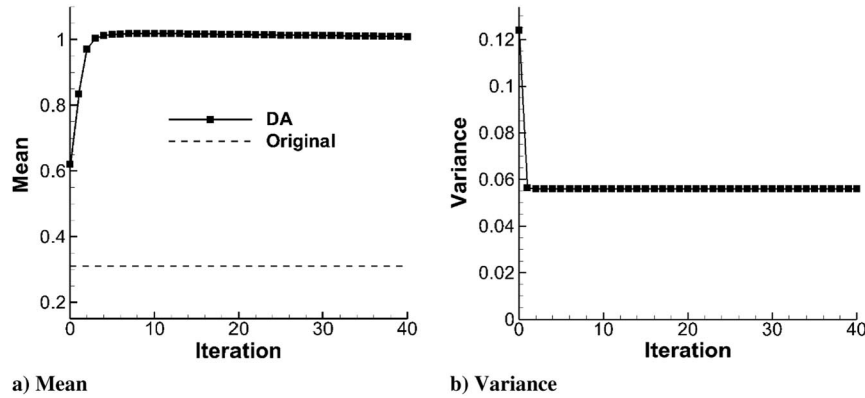

a) Mean   b) Variance
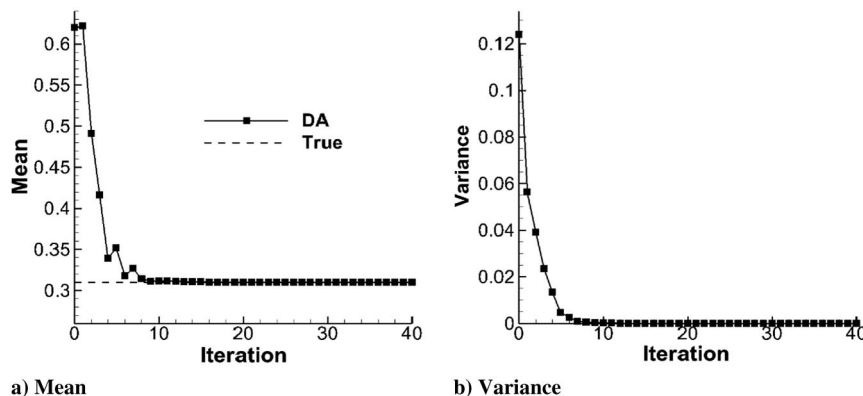
Fig. 6   Estimation histories of the mean and variance of the a_1 values of ensemble members.
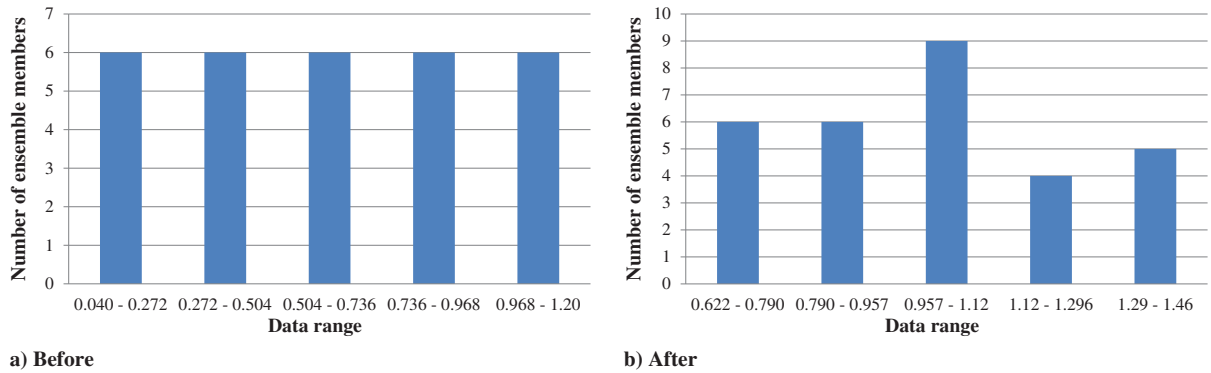
a) Before   b) After
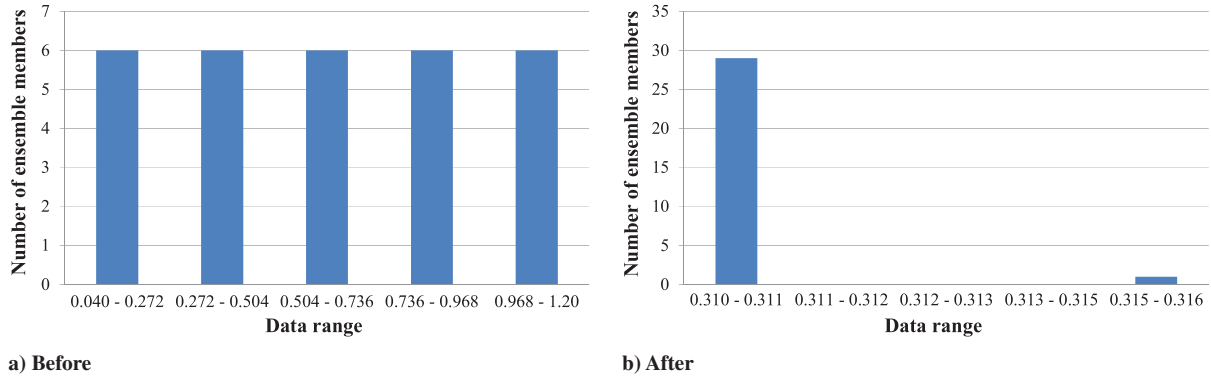
Fig. 7 Histograms of the a_1 values of the ensemble members before and after estimation in the numerical experiment. Note that the histogram intervals differ between Figs. 7a and 7b.

a) Mean   b) Variance

Fig. 8 Estimation histories of the mean and variance of the a_1 values of the ensemble members in the actual data assimilation.

a) Before   b) After

Fig. 9 Histograms of the a_1 values of the ensemble members before and after estimation in the actual data assimilation. Note that the histogram intervals differ between Figs. 9a and 9b.

This study adopts the mean of the estimated a_1 values as the representative value. In other words, the proposed data assimilation framework predicts 1.0 as the optimal value of a_1.

B. Demonstrations

To validate the effectiveness of the estimated parameter value, several flow problems were computed with a_1 set to 1.0, namely the flow over a backward-facing step and a flat-plate boundary layer, 2-D

Table 1   Ensemble means and variances of the a_1 values in the numerical experiment

Statistic	Before	After	True
Mean	0.620	0.310	0.310
Variance	1.24d-01	1.23d-06	— —

transonic flow around the RAE 2822 airfoil, and 3-D transonic flow around the ONERA M6 wing. The flow conditions were based on the corresponding cases in the National Program for Applications-Oriented Research in CFD (NPARC) verification and validation website¶ of NASA. The computations were conducted using FaSTAR and were implemented on the verified computational methods and grids. Note that the estimated value of a_1 in the demonstrations is expressed as 1.0 because the original estimate (0.31) is determined to two significant figures. In addition, computed results by the Menter baseline (BSL) turbulence model are shown in the validated flow problems. The difference between the SST model and the BSL model is the formulation of the turbulent eddy viscosity as shown in Eq. (1), and the BSL model does not include the max operator in the formulation of the turbulent eddy viscosity, unlike the SST model.

¶Data available online at http://www.grc.nasa.gov/WWW/wind/valid/.

Statistic	Before	After
Mean	0.620	1.01
Variance	1.24d-01	5.59d-02

1. Two-Dimensional Backward-Facing Step

The optimized a_1 is first demonstrated in flow over a backward-facing step, as reported by Driver and Seegmiller [8]. The flow conditions were those employed in the parameter estimation by data assimilation. The computational grid and methods employed in this calculation were also identical to those of the data assimilation and are described in Sec. II. Figure 10 compares the pressure and skin friction coefficients on the lower surface around the backward-facing step, and Fig. 11 compares the horizontal velocity profiles at four streamwise locations ($x/H = 1.0, 4.0, 6.0,$ and 10.0). Plotted in both figures are the experimental results and the computational results with $a_1 = 0.31$ and 1.0. The computed reattachment length is 6.4 and 5.9 for $a_1 = 0.31$ and 1.0, respectively, whereas the experimental length is 6.4 (Fig. 10). Moreover, the pressure and skin friction coefficients, as well as the horizontal velocity profiles, better match the experimental values when $a_1 = 1.0$ than when $a_1 = 0.31$. In addition, the results show that the SST-2003 model with $a_1 = 1.0$ and the BSL model predict almost the same results.

### 2. Two-Dimensional Zero Pressure Gradient Flat Plate

Next, the optimized a_1 was evaluated on a flat-plate boundary layer. The Reynolds number of the flow was 5 million (based on a

computational length of 1), and the Mach number was 0.2. These flow conditions match those of the 2-D zero pressure gradient flat-plate verification case in the turbulence modeling resource of NASA Langley Research Center.

In this computation, the inviscid flux term was computed by the Harten–Lax–van Leer–Einfeldt–Wada (HLLEW) scheme [22], and the time integration was implicitly performed by the lower/upper symmetric Gauss–Seidel implicit method [23]. The time integration was performed using local time stepping, and the gradients were calculated to second-order spatial accuracy by GLSQ with Hishida's limiter.

The computation ran on a three-dimensional (3-D) unstructured grid (two identical x-z planes separated by a distance $y = 1$, giving one spanwise cell for all grid levels). The computational grid comprised 419,650 nodes and 208,896 elements, and the minimum spacing of the surface normal in the wall units was approximately 5.0d-7. The grid employed in this computation is available in the turbulence modeling resource developed by NASA Langley Research Center. The effects of the minimum surface normal spacing on the computational results were investigated before computation.

Because this flow involves no complicated turbulent phenomena such as separation, reattachment, and adverse pressure gradient flows, it is accurately predicted by most turbulence models. The objective of this demonstration is to investigate whether setting $a_1 = 1.0$ in the computation predicts the boundary layer as accurately as setting $a_1 = 0.31$. Thanks to the formulation of the SST model, computations of flows without separation, reattachment, and adverse pressure gradient flows are considered to be independent of a_1. Figure 12 compares the logarithm of the theoretical and computational wall solutions for $a_1 = 0.31$ and 1.0 at the streamwise

a) Pressure coefficient   b) Skin friction coefficient
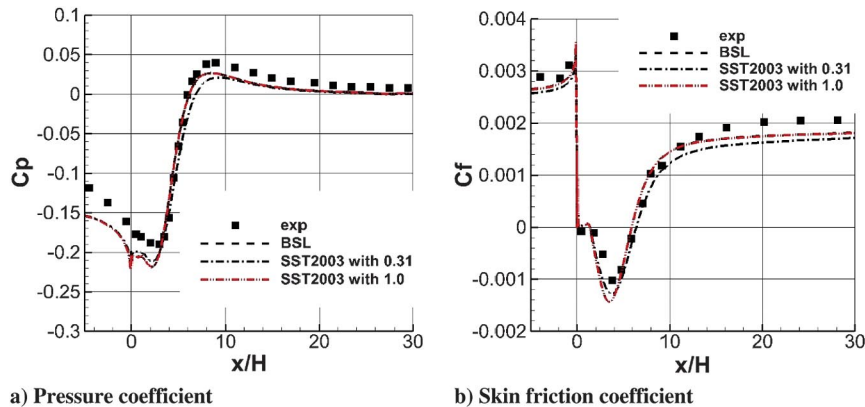
Fig. 10   Comparisons of pressure coefficients and skin friction coefficients on the lower surface around the backward-facing step.
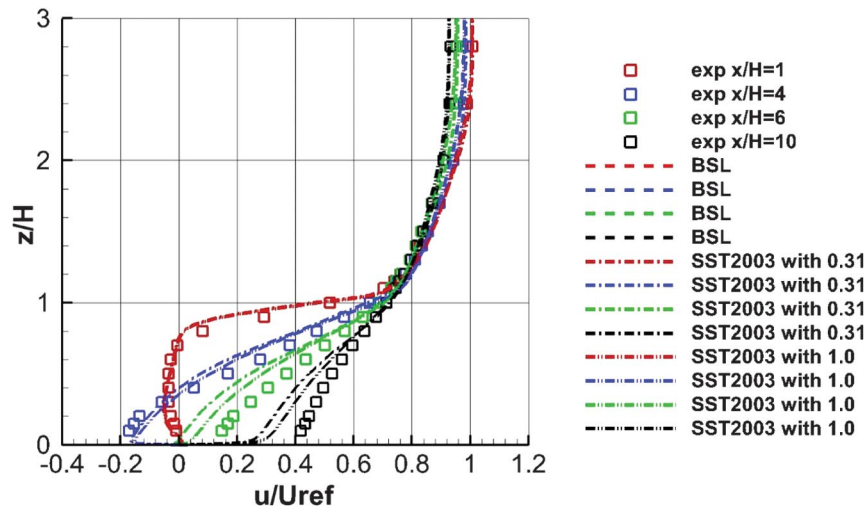
Fig. 11   Comparison of horizontal velocity profiles at the streamwise locations $x/H = 1.0, 4.0, 6.0,$ and 10.0.
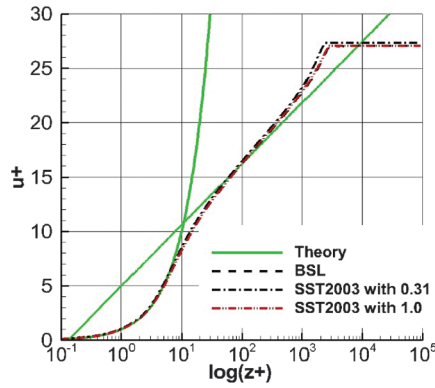
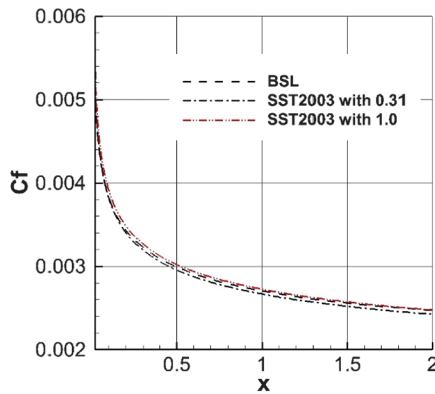**Fig. 12 Comparison of the logarithm of the wall solutions at the streamwise location $x/H = 0.97$.**

Fig. 13 Comparison of the skin friction coefficients.

position $x = 0.97$. The theoretical calculation assumes $\kappa = 0.41$ and $B = 5.0$. Both a_1 values yield almost identical results and are consistent with the theory. In addition, the results show that the SST-2003 model and the BSL model predict almost the same results.

Figure 13 compares the skin friction coefficients for $a_1 = 0.31$ and 1.0. The skin friction coefficients are insensitive to the parameter a_1 in this particular scenario.

3. Two-Dimensional Transonic Flow Around the RAE 2822 Airfoil

The third investigation was 2-D transonic flow around the RAE 2822 airfoil. The flow conditions were those adopted in the experimental study of Cook et al. [24]: Reynolds number = 6.5 million, Mach number = 0.729, and angle of attack = 2.31 deg. This flow is discussed in the NPARC verification and validation website of NASA, which reports that some turbulence models predict slightly different shock locations.
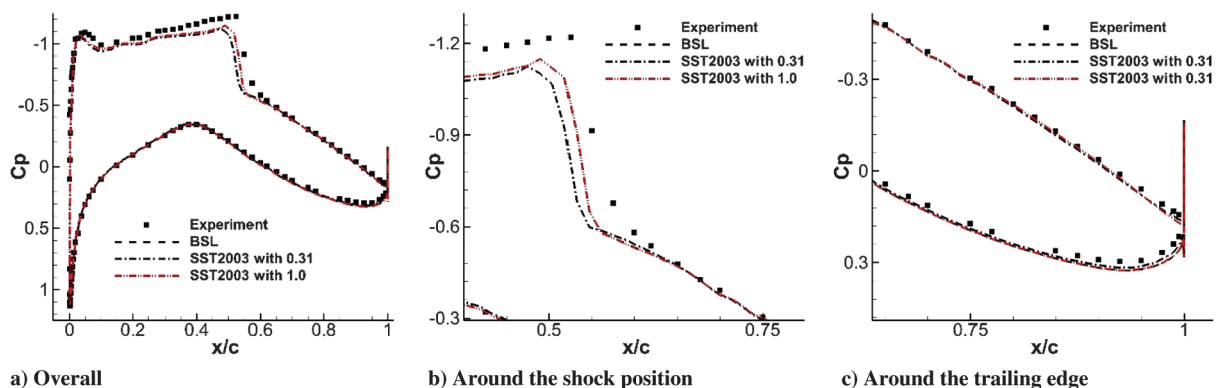
In this computation, the inviscid flux term was computed by HLLEW, and the generalized minimal residual (GMRES) implicit method [25] was implicitly performed for the time integration. The time integration was performed using local time stepping, and the gradients were calculated to second-order spatial accuracy by GLSQ with Hishida's limiter.

The computation run on a three-dimensional (3-D) unstructured grid (two identical x-z planes separated by a distance $y = 1$, giving one spanwise cell for all grid levels). The grid comprised 33,288 nodes and 16,425 elements, and the minimum spacing of the surface normal in the wall units was approximately 3.9d-6. The effects of the minimum surface normal spacing on the computational results were investigated before computation.

Figure 14 compares the computational and experimental pressure coefficients on the airfoil. The computations were performed by the SST-2003 model with a_1 set to 0.31 and 1.0. Although both computed shock positions precede the experimental one, the computed shock position better fits the experimental result when $a_1 = 1.0$ than when $a_1 = 0.31$. The pressure coefficients computed with $a_1 = 0.31$ and 1.0 are similar and noticeably differ only around the shock position. Figure 15 compares the computed skin friction coefficients on the airfoil. In this scenario, the computed skin friction coefficient is slightly larger for $a_1 = 1.0$ than for $a_1 = 0.31$. In addition, the results show that the SST-2003 model with $a_1 = 1.0$ and the BSL model predict almost the same results.

4. Three-Dimensional Transonic Flow Around the ONERA M6 Wing

Finally, the optimized a_1 is demonstrated on 3-D transonic flow around the ONERA M6 wing. The Reynolds number of the simulated flow was 11.72 million (based on the mean aerodynamic chord), and the Mach number was 0.8395. Computations were performed at two angles of attack (i.e., 3.06 and 6.06 deg).

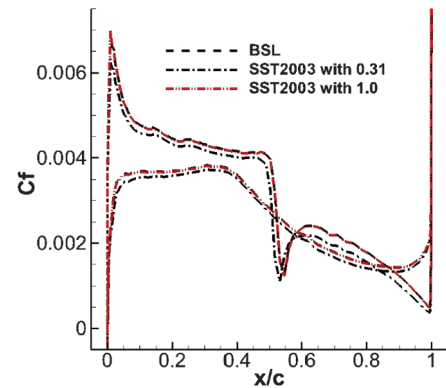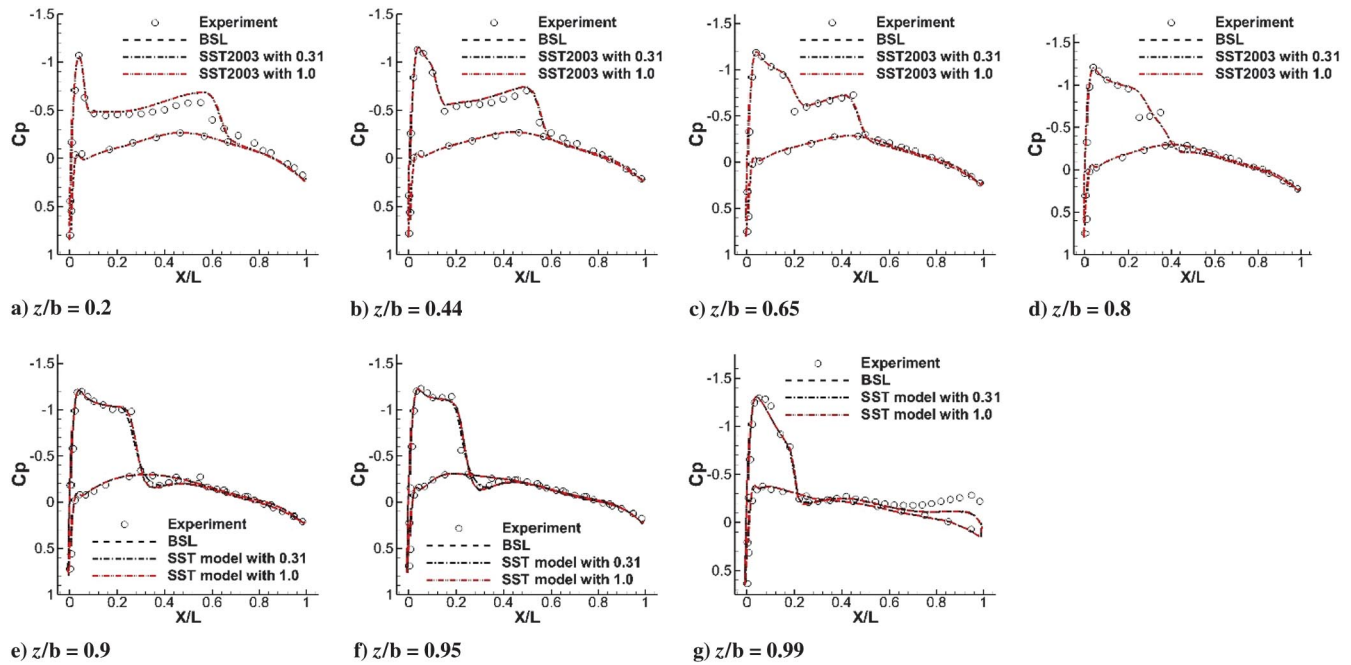**Fig. 15 Comparison of computed skin friction coefficients C_f on the RAE 2822 airfoil.**

a) Overall

b) Around the shock position

c) Around the trailing edge

Fig. 14 Comparisons of pressure coefficients C_p on the RAE 2822 airfoil.

a) $z/b = 0.2$ b) $z/b = 0.44$ c) $z/b = 0.65$ d) $z/b = 0.8$

e) $z/b = 0.9$ f) $z/b = 0.95$ g) $z/b = 0.99$

Fig. 16   Comparison of pressure coefficients around the ONERA M6 wing (angle of $\mathrm{attack} = 3.06$ deg). Figure 16b is the wingspan length.

a) $z/b = 0.2$ b) $z/b = 0.44$ c) $z/b = 0.65$ d) $z/b = 0.8$

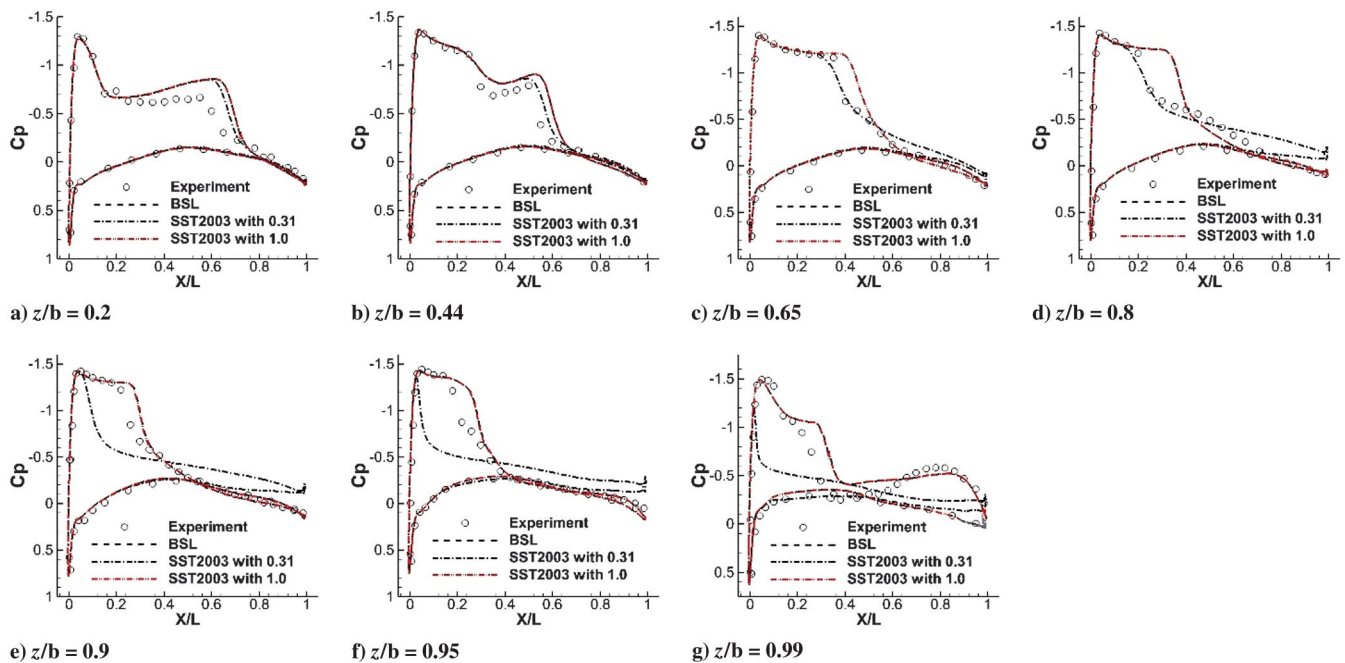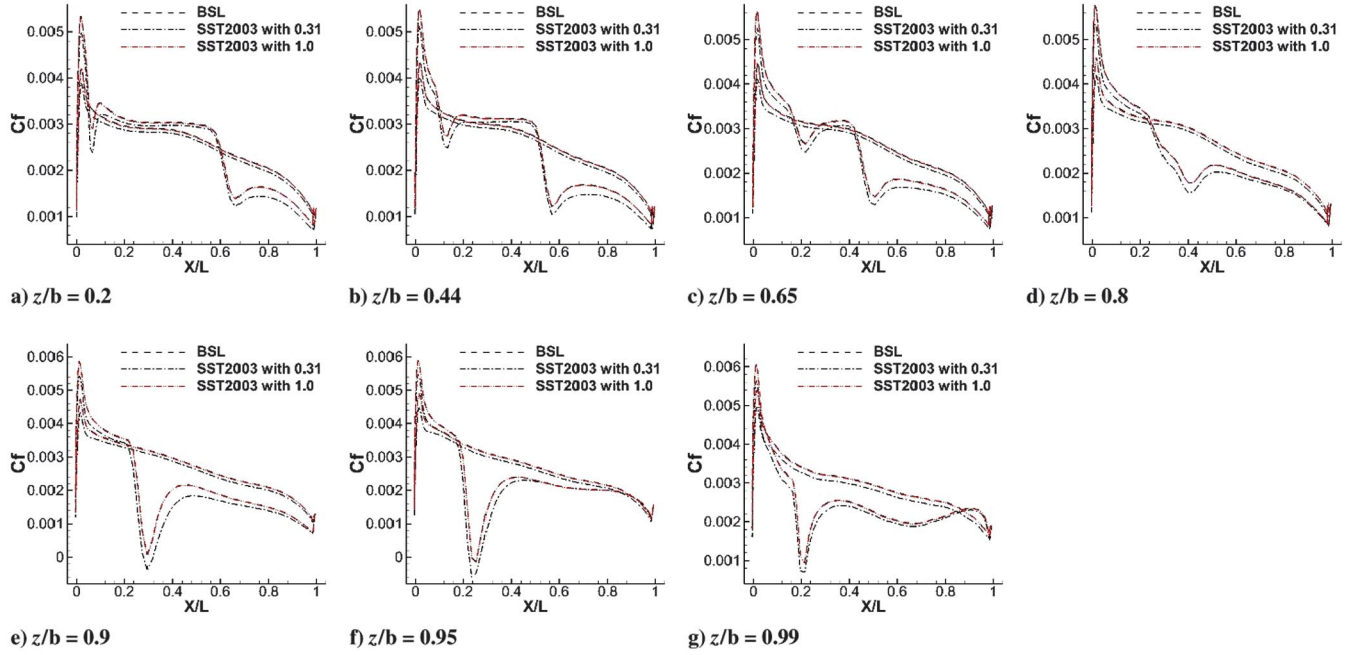e) $z/b = 0.9$ f) $z/b = 0.95$ g) $z/b = 0.99$

Fig. 17   Comparison of pressure coefficients around the ONERA M6 wing (angle of $\mathrm{attack} = 6.06$ deg). Figure 17b is the wingspan length.

In this computation, the inviscid flux term was computed by HLLEW, and the GMRES was implicitly performed for the time integration. The time integration was performed using local time stepping, and the gradients were calculated to second-order spatial accuracy by GLSQ with Hishida's limiter.

The computation ran on a three-dimensional (3-D) unstructured grid. The grid comprised 678,053 nodes and 663,264 elements, and the minimum spacing of the surface normal in the wall units was approximately 9.8d-6. The effects of the minimum surface normal spacing on the computational results were investigated before computation.

The experimental data were reported by Schmitt and Charpin [26]. The flow for the 3.06 deg angle of attack is discussed in the NPARC verification and validation website of NASA. At this angle of attack, the flow is considered to involve a separation. Figures 16 and 17

compare the computed and experimental pressure coefficients at seven sections on the wing surface for angle of attack = 3.06 and 6.06 deg, respectively. The computations were conducted by the SST2003 model with $a_1 = 0.31$ and 1.0. The computational results at 3.06 deg are essentially independent of a_1 (Fig. 16). On the other hand, at the higher angle of attack, the computational results strongly depend on a_1, and the pressure coefficient around the wing tip for $z/b \geq 0.9$ better fits the experimental data when $a_1 = 1.0$ than when $a_1 = 0.31$ (Fig. 17). On the other hand, for $z/b < 0.9$, setting $a_1 = 1.0$ yields no apparent improvement in the modeled data. Apart from the trailing edge, the pressure coefficients on the upper wing surface do not better capture the experimental values when $a_1 = 1.0$ than when $a_1 = 0.31$. Figures 18 and 19 compare the computed skin friction coefficients at seven sections for the angle of attack = 3.06 and 6.06 deg, respectively. At the smaller angle of attack, the

Fig. 18   Comparison of computed skin friction coefficients around the ONERA M6 wing (angle of attack = 3.06 deg). Figure 18b is the wingspan length.
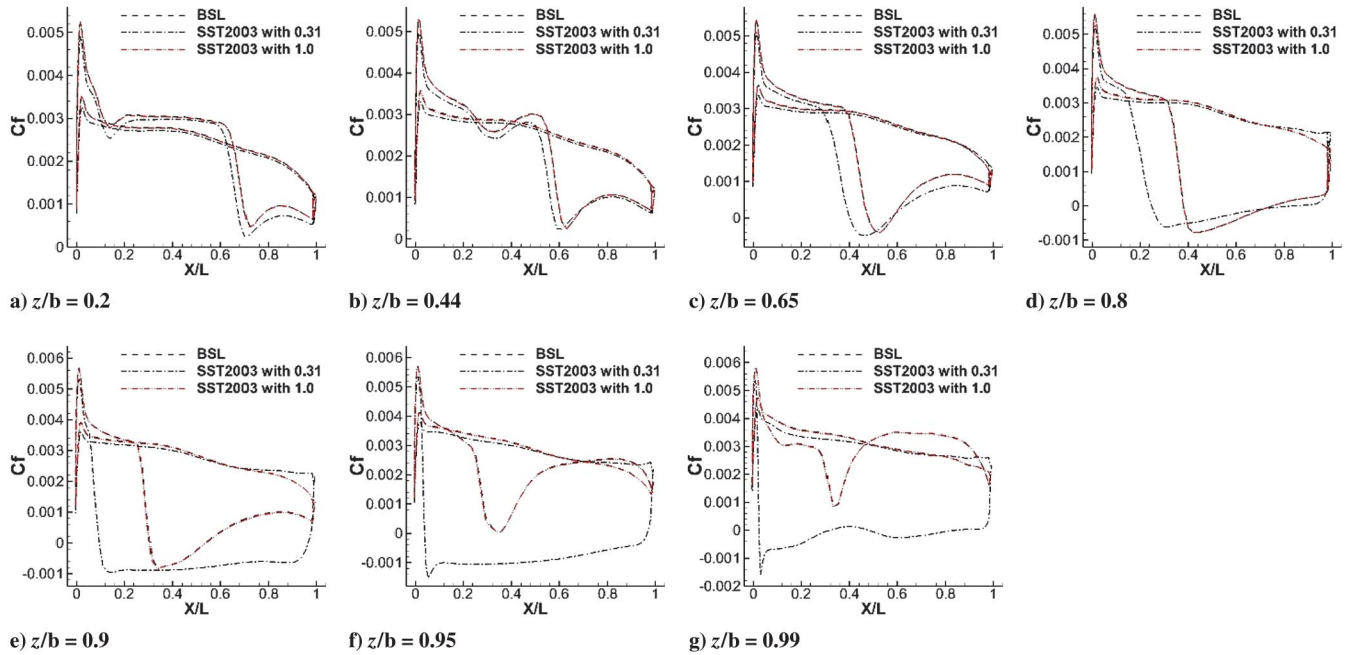
Fig. 19   Comparison of computed skin friction coefficients around the ONERA M6 wing (angle of attack = 6.06 deg). Figure 19b is the wingspan length.

computed skin friction coefficients are slightly larger when $a_1 = 1.0$ than when $a_1 = 0.31$. At the larger angle, this trend holds only for $z/b < 0.65$; when $z/b \geq 0.65$, the computed skin friction coefficients are largely different between $a_1 = 1.0$ and 0.31. In this case, setting $a_1 = 1.0$ does not yield a separation flow for $z/b \geq 0.95$, where the skin friction coefficient becomes positive, unlike setting $a_1 = 0.31$. In addition, the results show that the SST-2003 model with $a_1 = 1.0$ and the BSL model predict almost the same results.

IV.   Conclusions

This study has proposed a data assimilation methodology for estimating the optimum parameter values of turbulence models. The proposed method was applied to estimate the value of a_1 in the Menter k-ω SST turbulence model (the SST-2003 model), which was

modified by Menter in 2003. Given the true value of a_1, the effectiveness of optimizing a_1 in the SST-2003 model by data assimilation was numerically investigated. Applying data assimilation to flows over a backward-facing step, a_1 was determined as 1.0. The effectiveness of the estimated parameter value was validated in computations of several flows: flows over a 2-D backward-facing step and a 2-D flat-plate boundary layer, 2-D transonic flow around the RAE 2822 airfoil, and 3-D transonic flows around the ONERA M6 wing. The validation results are summarized next.

1) In the absence of separation and adverse pressure gradient flows, the predictions of the SST-2003 model with $a_1 = 1.0$ (the optimized value) and $a_1 = 0.31$ (the original value) are almost the same.

2) Setting a_1 to 1.0 rather than 0.31 improves the SST-2003 model in separated or adverse pressure gradient flows, as evidenced by the

better match between the computational and experimental results when $a_1 = 1.0$ than when $a_1 = 0.31$.

These observations suggest that the proposed data assimilation methodology effectively optimizes the parameter values of turbulence models. The SST-2003 model performed more effectively when $a_1 = 1.0$ than when $a_1 = 0.31$. Therefore, the improvement of the Menter SST turbulence model has been confirmed by adopting a much simpler approach than previous efforts, which have modified the model formulas.

Moreover, the comparison results between the BSL model and the SST-2003 model with $a_1 = 1.0$ are suggested next.

1) 0.31 is too low a value as the parameter value of a_1. When $a_1 = 0.31$, SF_2 as shown in Eq. (8) tends to be adopted improperly as the denominator of the formulation of the turbulent eddy viscosity. As the result, the shear-stress transport term in the SST-2003 model for applications with adverse pressure gradient flows does not work well.

2) Setting a_1 to 1.0 from 0.31 can resolve the preceding problem. When $a_1 = 1.0$, $a_1\omega$ as shown in Eq. (8) is adopted properly as the denominator of the formulation of the turbulent eddy viscosity, and the SST-2003 model becomes almost the same as the BSL model, which always adopts ω as the denominator of the formulation of the turbulent eddy viscosity.

It should be noted that these observations cannot suggest that the shear-stress transport term in the SST-2003 model is not always required for applications with adverse pressure gradient flows because there is no flow problem that the SST-2003 model with $a_1 = 0.31$ predicts better result than the BSL model in the demonstrations.

However, there is a remaining issue to be resolved. The issue is that the SST-2003 model is inherently imperfect because it is essentially a linear eddy-viscosity-type turbulence model. Such models are widely used in engineering applications of CFD, but they ignore the nonlinear effects of turbulent flow. The nonlinear effect is prominent in certain regions such as the wing root. In fact, the SST-2003 model could not capture the experimental values around the root of the ONERA M6 wing, even when $a_1 = 1.0$. Therefore, to more accurately reproduce the physical phenomena, high-fidelity nonlinear turbulence models should be employed, such as the SA model with quadratic constitutive relation, proposed by Spalart in 2000 [27].

Finally, the possibility of optimization by the data assimilation methodology must be mentioned. This study optimized a single parameter through 2-D simulations. However, the data assimilation methodology can potentially optimize multiple parameters, including the initial and boundary conditions. Although the applicability of data assimilation methodology is limited by the large computational resources and high performance demands, these problems are becoming solvable with modern advances in computational technology. These observations suggest that the data assimilation methodology might optimize other complicated problems, such as many-parameter problems and 3-D situations. In particular, the authors are interested in applying this optimization procedure to combustion models and chemical kinetic models, which are characterized by numerous empirically determined parameter values and complex physical phenomena. By optimizing as many parameters as possible in these models, the model performance could be improved and complicated physical phenomena better understood. With this understanding, fluid machines with unprecedented performance capabilities could be designed.

Acknowledgments

References

[1] Spalart, P. R., "A One-Equation Turbulence Model for Aerodynamic Flows," *30th Aerospace Sciences Meeting and Exhibit*, AIAA Paper 1992-0439, 1992.

[2] Menter, F. R., "Two-Equation Eddy-Viscosity Turbulence Models for Engineering Applications," *AIAA Journal*, Vol. 32, No. 8, 1994, pp. 1598–1605.
doi:10.2514/3.12149

[3] Menter, F. R., Kuntz, M., and Langtry, R., "Ten Years of Industrial Experience with the SST Turbulence Model," *Turbulence, Heat and Mass Transfer 4*, Begell House, Danbury, CT, 2003, pp. 625–632.

[4] Edeling, W. N., Cinnella, P., Dwight, R. P., and Bijl, H., "Bayesian Estimates of Parameter Variability in the Turbulence Model," *Journal of Computational Physics*, Vol. 258, Feb. 2014, pp. 73–94.
doi:10.1016/j.jcp.2013.10.027

[5] Johnson, D. A., and King, L. S., "A Mathematically Simple Turbulence Closure Model for Attached and Separated Turbulent Boundary Layers," *AIAA Journal*, Vol. 23, No. 11, 1985, pp. 1684–1692.
doi:10.2514/3.9152

[6] Wunsch, C., *The Ocean Circulation Inverse Problem*, Cambridge Univ. Press, Cambridge, U.K., 1996.

[7] Bishop, C. H., Etherton, B. J., and Majumdar, S. J., "Adaptive Sampling with the Ensemble Transform Kalman Filter. Part 1: Theoretical Aspects," *Monthly Weather Review*, Vol. 129, No. 3, 2001, pp. 420–436.
doi:10.1175/1520-0493(2001)129<0420:ASWTET>2.0.CO;2

[8] Driver, D. M., and Seegmiller, H. L., "Features of Reattaching Turbulent Shear Layer in Divergent Channel Flow," *AIAA Journal*, Vol. 23, No. 2, 1985, pp. 163–171.
doi:10.2514/3.8890

[9] Eça, L., Hoekstra, M., Roache, P. J., and Coleman, H. W., "Code Verification, Solution Verification and Validation: An Overview of the 3rd Lisbon Workshop," *19th AIAA Computational Fluid Dynamics Conference*, AIAA paper 2009-3647, June 2009.

[10] Evensen, G., "Sequential Data Assimilation with a Nonlinear Quasi-Geostrophic Model Using Monte Carlo Methods to Forecast Error Statistics," *Journal of Geophysical Research*, Vol. 99, No. C5, 1994, pp. 10,143–10,162.

[11] Kitagawa, G., "Monte Carlo Filter and Smoother for Non-Gaussian Nonlinear State Space Models," *Journal of Computational and Graphical Statistics*, Vol. 5, No. 1, 1996, pp. 1–25.
doi:10.2307/1390750

[12] Talagrand, O., and Courtier, P., "Variational Assimilation of Meteorological Observations with the Adjoint Vorticity Equation 1: Theory," *Quarterly Journal of the Royal Meteorological Society*, Vol. 113, No. 478, 1987, pp. 1311–1328.
doi:10.1002/qj.49711347812

[13] Hashimoto, A., Murakami, K., Aoyama, T., Ishiko, K., Hishida, M., Sakashita, M., and Lahur, P., "Toward the Fastest Unstructured CFD Code 'FaSTAR'," *50th AIAA Aerospace Sciences Meeting*, AIAA Paper 2012-1075, Jan. 2012.

[14] Shima, E., and Kitamura, K., "On New Simple Low-Dissipation Scheme of AUSM-Family for All Speeds," *47th AIAA Aerospace Sciences Meeting*, AIAA Paper 2009-0136, Jan. 2009.

[15] Yamamoto, S., "Preconditioning Method for Condensate Fluid and Solid Coupling Problems in General Curvilinear Coordinates," *Journal of Computational Physics*, Vol. 207, No. 1, 2005, pp. 240–260.
doi:10.1016/j.jcp.2005.01.013

[16] Shima, E., Kitamura, K., and Fujimoto, K., "New Gradient Calculation Method for MUSCL Type CFD Schemes in Arbitrary Polyhedra," *48th AIAA Aerospace Sciences Meeting*, AIAA Paper 2010-1081, Jan. 2010.

[17] Kalman, R. E., "A New Approach to Linear Filtering and Prediction Problems," *Journal of Basic Engineering*, Vol. 82, No. 1, 1960, pp. 35–45.
doi:10.1115/1.3662552

[18] Anderson, B. D. O., and Moore, J. B., *Optimal Filtering*, Prentice–Hall, Upper Saddle River, NJ, 1979.

[19] Evensen, G., "Using the Extended Kalman Filter with a Multilayer Quasi-Geostrophic Ocean Model," *Journal of Geophysical Research*, Vol. 97, No. C11, 1992, pp. 17,905–17,924.
doi:10.1029/92JC01972

[20] Potter, J. E., and Stern, R. G., "Statistical Filtering of Space Navigation Measurements," *AIAA Guidance and Control Conference*, AIAA Paper 1963-333, Aug. 1963.

[21] Nerger, L., Janjić, T., Schröter, J., and Hiller, W., "A Unification of Ensemble Square Root Kalman Filters," *Monthly Weather Review*, Vol. 140, No. 7, 2012, pp. 2335–2345.
doi:10.1175/MWR-D-11-00102.1

[22] Obayashi, S., and Guruswamy, G. P., "Convergence Acceleration of a Navier–Stokes Solver for Efficient Static Aeroelastic Computation," *AIAA Journal*, Vol. 33, No. 6, 1995, pp. 1134–1141.
doi:10.2514/3.12533

[23] Sharov, D., and Nakahashi, K., "Reordering of Hybrid Unstructured Grids for Lower–Upper Symmetric Gauss–Seidel Computations," *AIAA*

Journal, Vol. 36, No. 3, 1998, pp. 484–486.
doi:10.2514/2.392

[24] Cook, P. H., McDonald, M. A., and Firmin, M. C. P., "Aerofoil RAE 2822: Pressure Distributions, and Boundary Layer and Wake Measurements," AGARD Rept. AR-138, Neuilly sur Seine, France, 1979.

[25] Saad, Y., and Schultz, M. H., "GMRES: A Generalized Minimal Residual Algorithm for Solving Nonsymmetric Linear Systems," *SIAM Journal on Scientific and Statistical Computing*, Vol. 7, No. 3, 1986, pp. 856–869.
doi:10.1137/0907058

[26] Schmitt, V., and Charpin, F., "Pressure Distributions on the ONERA-M6-Wing at Transonic Mach Numbers," AGARD Rept. AR-138, Neuilly sur Seine, France, 1979.

[27] Spalart, P. R., "Strategies for Turbulence Modelling and Simulation," *International Journal of Heat and Fluid Flow*, Vol. 21, No. 3, 2000, pp. 252–263.
doi:10.1016/S0142-727X(00)00007-2

J. Sahu
Associate Editor